Host-Guest Synergy of $CH_3NH_3PbBr_3$@Ln-MOFs Enabling Tunable Green Luminescence and Switchable Memory

Liming Zhao[a], Carl Redshaw[b], Kuixing Ding[c], Pengyue Zhang[a,*], Bin Chen[d], Zhirong Chen,[d] Jiugang Hu[c,*] and Haohong Li[d,*]

[a] College of Standardization, China Jiliang University, Hangzhou 310018, China.

[b] Department of Chemistry & Biochemistry, University of Hull, Hull, HU6 7RX, UK.

[c] College of Chemistry and Chemical Engineering, Central South University, Changsha, 410083, China.

[d] College of chemistry, Fuzhou University, Fuzhou, Fujian, 350116, China.

Highlights

- New Ln-MOFs can serve as multifunctional platforms.
- Low cost $CH_3NH_3PbBr_3$@Ln-MOFs show tunable luminescence behaviour.
- $CH_3NH_3PbBr_3$@Sm-MOF exhibits excellent electrical bistability behaviour with high ON/OFF ratio of 10^4.
- $CH_3NH_3PbBr_3$@Ln-MOFs can be utilized as a new generation of photovoltaic, light-emitting, and switching memory devices.

Abstract: Perovskite $CH_3NH_3PbBr_3$ nanoparticles (NPs) can be intercalated into diverse porous materials to expand the flexibility and versatility of the host-guest composites due to their outstanding optical properties. Herein, by encapsulating $CH_3NH_3PbBr_3$ NPs into lanthanide metal organic frameworks (Ln-MOFs), four $CH_3NH_3PbBr_3$@Ln-MOFs composites, namely $\{[Ln(BTB)(H_2O)_2]\cdot 3(H_2O)\}_n$ (Ln=La, Nd, Pr, Sm), have been fabricated and can serve as multifunctional platforms. The temperature-dependent luminescence properties of the $CH_3NH_3PbBr_3$@Ln-MOFs with different concentrations of $CH_3NH_3PbBr_3$ were explored and the results revealed tuneable green luminescence. In particular, the $CH_3NH_3PbBr_3$@Sm-MOF exhibits a variety of colours from green to blue to purple and an excellent quantum yield (0.987) on addition of 1.0 mmol $PbBr_2$. The photocurrent responses of the $CH_3NH_3PbBr_3$@Ln-MOFs reveal the enhancement mechanism of $CH_3NH_3PbBr_3$ on charge-hole separation. Moreover, owing to its unique properties, the electrical bistability behaviour with a high ON/OFF ratio of 10^4 was observed for the $CH_3NH_3PbBr_3$@Sm-MOF. The electron transfer mechanism was verified by theoretical calculations. Hence, the $CH_3NH_3PbBr_3$@Ln-MOFs composites are promising candidates for a new generation of photovoltaic, light-emitting and switching memories devices.

Keywords: perovskite nanoparticles; host-guest composites; electrically bistability; lanthanide metal-organic framework; switching memories devices

1. Introduction

Metal organic frameworks (MOFs) are a type of porous crystalline material that are attracting much attention. Much of the interest stems from their adjustable pore sizes and high specific surface area, and they can be easily designed and self-assembled [1]. The unique electronic structure and special properties of Lanthanide (Ln) metals determine that they have important basic and applied research significance. These properties are different from those of main group and transition metal species because of their 4f sub-electron layer structures and outer 5s, $5p^6$ electron shielding, which can produce specific physical and chemical properties after receiving energy radiation [2]. Meanwhile, the Ln central ions could obtain more coordination field stabilization energy and reduce the mutual repulsion between outer orbital and ligand electrons. Therefore, lanthanide metal organic frameworks (Ln-MOFs) can achieve more stable complexes with oxygen-containing ligands through the energy transfer between ligands and central ions, leading to special photoelectric properties.

As crystalline porous materials, MOFs contain ordered pores capable of encapsulating varied types of guest, including metal NPs [3], dye molecules [4], polyoxometalates [5], metal oxide [6] and quantum dots (QDs) [7]. In these systems, MOFs can provide a platform for the stabilization of guests without reducing the wide range of properties that traditional guests exhibit. Therefore, host-guest composites have shown potential for various applications such as temperature sensing [8], luminescent thermometers [9] and in second-order non-linear optics [10]. It is noteworthy that inorganic QDs such as CdS, CdSe, CdTe, and ZnS have been successfully

encapsulated into MOFs to form QDs@MOFs, and a range of potential applications have been investigated such as for energy production [11], light harvesting [12], light emitting diode (LED) [13], and supercapacitors [14]. At present, research on QDs has mainly focused on classical cadmium-based semiconductor materials, which generally adopt a thick core-shell structure and are complicated to prepare. Any industrial use of these materials must overcome challenges such as cost and environmental issues to become attractive. Among the large families of QDs available, the halide perovskites $MPbX_3$ ($M = CH_3NH_3$; X = Cl, Br, I) NPs are attractive owing to their low cost, superior photoelectronic properties and multifunctional applications, and have been widely considered as central to forming a new generation of luminescent [15], solar cells [16], and memory storage materials [17].

As we know, the luminescence performance of MOF encapsulated QDs at room temperature has widely been studied [18], but the dependence of the luminescence of these composites under special/harsh environments, especially at extreme temperature has rarely been reported. In general, hybrid $CH_3NH_3PbX_3$ NPs can exhibit excellent photoluminescence intensity and quantum yields with adjustable emission depending on the halide anions. Moreover, these perovskite NPs exhibit thermal dependence, emitting photoluminescence at room temperature and quenching as the temperature rises to a certain temperature [18c]. Moreover, $CH_3NH_3PbX_3$ NPs have the advantage of long lifetime of direct-band gap carriers. The low density of states and the sharp energy level of nanoscale QDs can produce three-dimensional quantum confinement effects on the carriers in them, and they can can be used as stable charge capture sites, which is

beneficial to prolonging the life of a memory device. However, for the pure perovskite, it was found that the high resistance state of the memory device decreases and overlaps with the low resistance state on increasing the number of cycles [19]. This phenomenon is attributed to a space-charge-limited conduction mechanism predominantly of electric bistable. Hence, encapsulating the perovskite NPs into a MOF can potentially prevent the formation of halogen vacancy and improve the cyclic stability of the device. In addition, this method can improve the stability of perovskite films and enlarge the switching window.

Based on the above, by encapsulating $CH_3NH_3PbBr_3$ NPs into Ln-MOFs, four $CH_3NH_3PbBr_3$@Ln-MOFs composites, namely $\{[Ln(BTB)(H_2O)_2]\cdot 3(H_2O)\}_n$ (Ln=La, Nd, Pr, Sm), have been fabricated and shown to serve as a multifunctional platform. The temperature luminescence dependence of $CH_3NH_3PbBr_3$@Sm-MOF with different concentrations of $CH_3NH_3PbBr_3$ was studied. The I-V characteristics of the ITO/$CH_3NH_3PbBr_3$@Sm-MOF/Ag film at -5 V to 5 V under a DC voltage were also analyzed. Moreover, the changes of the interface electron transfer and main structure of the composites were analyzed with the assistance of theoretical simulations of the properties of the composites.

2. Experimental section

2.1 Materials and Physical Measurements

All reagents were commercially purchased from Aladdin and were used without further purification. The diffraction intensity data of the single crystals were obtained

by using a Bruker APEX II CCD area diffractometer equipped with a fine focus, 2.0 kW sealed tube X-ray source (Mo Kα radiation, λ = 0.71073 Å) operating at 177 K. Infrared (IR) spectra were recorded on a Nicolet IS 50 FT-IR spectrometer using ATR in the range 400-4000 cm^{-1}. Powder X-ray diffraction (PXRD) patterns were performed on a Philips X'Pert-MPD diffractometer with CuKα radiation (λ = 1.54056 Å). Thermal gravimetric analysis (TGA) data were obtained using a Mettler Toledo TGA/DSC 3+ thermal analyzer, heating from 30 to 800 ºC at the constant rate 10 ºC/min under a nitrogen atmosphere. Transmission electron microscope (TEM) images were obtained on a FEI Talos F200S G2 at 200 kv. HR-SEM10 of sandwich films were tested on a Verios G4 UC. Fluorescence microscopic images were taken on MF-UV-LED-Y-3. Optical diffuse reflectance spectra were measured on an Aglient Carry 5000 UV/Vis/near-IR spectrophotometer equipped with an integrating sphere at 293 K and a $BaSO_4$ plate was used as a reference over the range of 250-800 nm. Fluorescence spectra were recorded on an Edinburgh FL-FS 920 TCSPC spectrometer.

2.2 Synthetic Procedures

The traditional precursor $PbBr_2$@MOFs were prepared in one-step by using solvothermal methods [7a]. The newly synthesized Ln-MOFs were immersed in $PbBr_2$ solution and were used as the precursor after subsequent washing and drying to prevent Pb ions from participating by coordination during the solvothermal reaction (**Scheme1**).

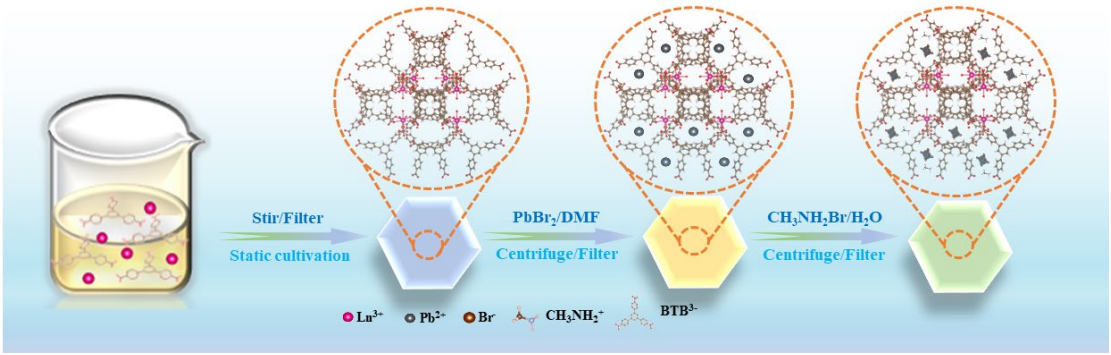

Scheme1. Illustration of the fabrication process of $CH_3NH_3PbBr_3$@Ln-MOFs.

***Synthesis of* Lanthanide metal–organic frameworks (Ln-MOFs)**

***Synthesis of* $\{[Ln(BTB)(H_2O)_2]\cdot 3(H_2O)\}_n$** ((Ln=La, Nd, Sm, Er) The four Ln-MOFs are isostructural, and were synthesized in the same way except that different lanthanide salts were employed. Using La-MOF as an example:

$\{[La(BTB)(H_2O)_2]\cdot 3(H_2O)\}_n$ (La-MOF): A mixture of H_3BTB(0.043 g, 0.1 mmol) and $La(NO_3)_3\cdot 6H_2O$ (0.065 g, 0.15 mmol) was dissolved in 8.0 ml DMF, and the system was stirred for 4h at 80℃ and then filtered. After two weeks, block crystals were obtained, which were washed with DMF and dried under vacuum for 24 h (0.051 g, yield 43.9% based on La). For $C_{27}H_{15}LaO_{12}$ (670.3): calculated C 48.38%, H 2.26 %; determined C 48.80%, H 2.10 %. IR (cm^{-1}): 1643(m), 1582(s), 1520(s), 1396(s), 1245(w), 1178(w), 1108(m), 1010(w), 861(s), 815(m), 775(s), 704(m), 664(m), 553(w), and 457(m).

$\{[Pr(BTB)(H_2O)_2]\cdot 3(H_2O)\}_n$ (Pr-MOF): Block greyish-green crystals were obtained (0.055g, yield 46.8 % based on Pr). For $C_{27}H_{15}PrO_{12}$ (672.3): calculated C 48.24%, H 2.25 %; determined C 48.50%, H 2.18 %. IR (cm^{-1}): 1643(m), 1582(s), 1520(s), 1396(s), 1245(w), 1178(w), 1108(m), 1010(w), 861(s), 815(m), 775(s), 704(m), 664(m), 553(w),

and 457(m).

{[Nd(BTB)(H_2O)$_2$]·3(H_2O)}$_n$ (Nd-MOF): Block light purple crystals, (0.05 g, yield: 43.2 % based on Nd). For $C_{27}H_{15}NdO_{12}$(675.63): calculated C 47.99%, H 2.24 %; determined C 48.10%, H 2.20 %. IR (cm^{-1}): 1643(m), 1582(s), 1520(s), 1396(s), 1245(w), 1178(w), 1108(m), 1010(w), 861(s), 815(m), 775(s), 704(m), 664(m), 553(w), and 457(m).

{[Sm(BTB)(H_2O)$_2$]·3(H_2O)}$_n$ (Sm-MOF): Block colorless crystals, yield 0.059 g 47.2 %. For $C_{27}H_{15}SmO_{12}$ (681.75): calculated C 47.57%, H 2.24 %; determined C 47.82%, H 2.18 %. IR (cm^{-1}): 1643(m), 1582(s), 1520(s), 1396(s), 1245(w), 1178(w), 1108(m), 1010(w), 861(s), 815(m), 775(s), 704(m), 664(m), 553(w), and 457(m).

***Synthesis of* PbBr$_2$@Ln-MOFs Composites:** The PbBr$_2$@Ln-MOFs composites were initially synthesized as the precursor of $CH_3NH_3PbBr_3$@Ln-MOFs. 50 mg La-MOFs were dispersed into different concentrations of $PbBr_2$ (0.1, 0.5 and 1.0 mmol dissolved in 5 ml DMF), respectively. After half an hour of ultrasonic treatment, the suspension was allowed to stand for 6 h, and was then centrifuged. The supernatant was filtered, and the product was washed with DMF several times. Finally, the product was dried at 60℃ for 12h.

***Synthesis of* $CH_3NH_3PbBr_3$@Ln-MOFs Composites:** The PbBr$_2$@Ln-MOF precursors were added into 5 mL deionized water containing CH_3NH_3Br (11.2 mg, 0.1 mmol), which after 30 min led to the formation of $CH_3NH_3PbBr_3$@MOFs composites. The supernatant was filtered, and the product was washed with deionized water several times. Finally, the products were dried at 60℃ for 12 h.

3. Results and Discussion

3.1 Structural Description of Ln-MOFs

Crystallographic analysis confirmed that all the Ln-MOFs are isostructural and crystalized in the Tetragonal system with space group *I4122* (Table S1). Here, the structure of $\{[Sm(BTB)(H_2O)_2]\cdot 3H_2O\}_n$ is described as an example. The 3D network comprises Sm_2O_{18} building blocks (**Figure 1a**) and BTB^{3-} ligands. The asymmetric unit of **Sm-MOF** contains one Sm(III) ion, one BTB ligand, two coordinated H_2O molecules and three isolated H_2O molecules. In each Sm_2O_{18} building block, the crystallographically independent Sm(III) center is coordinated by eight O donors which formed a twisted single-capped square anti-prismatic polyhedron (SmO_9), including six O atoms of BTB^{3-} ligands and two O atoms of coordinated H_2O molecules (**Figure 1b**). The Sm-O bond distances are normal at 2.390(7) to 2.646(6) Å, while the O-Sm-O angles ranging from 49.1(2) to 142.6(2)° account for the observed distorted (**Table S2**). The Sm_2O_{18} are connected via the same C atoms from the BTB^{3-} ligands, which results in a 1D chain (**Figure S1**). The chains are further interlinked into a 3D structure via bridging BTB^{3-}, and there are two types of coordination modes exhibited by the carboxylic groups of BTB^{3-}, namely bidentate chelate and bridged, respectively (**Figure S2**). Finally, the 3D network for **Sm-MOF** is displayed along both the *c* and *b* axes (**Figure 1c, d**), revealing the pores in the cage-like structure with sizes of 8.0 Å, which provides the possibility of encapsulating $CH_3NH_3PbBr_3$ perovskite nanoparticles into these Ln-MOFs. In order to better understand the structure, a simplified 3-D network

of **Sm-MOF** based on bridging BTB ligand Sm_2O_{18} nodes is presented in **Figure 1e**.

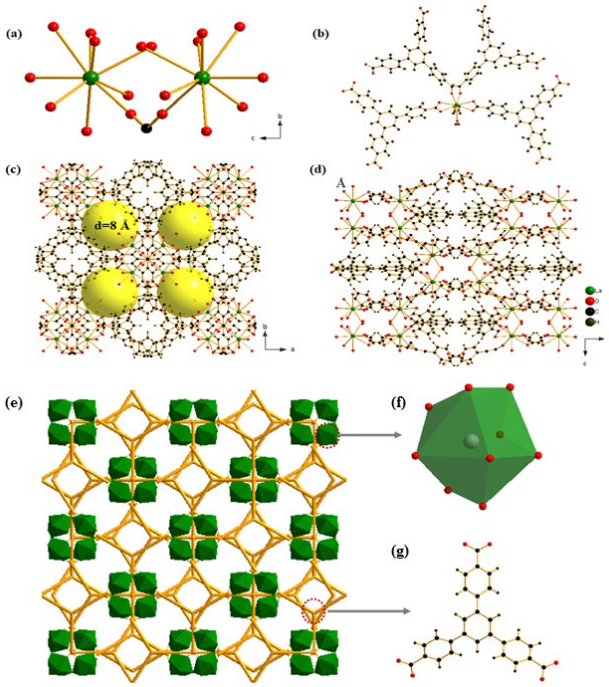

Figure 1. (a) Sm_2O_{18} building blocks; (b) Coordination environment at the Sm(III) ion; (c, d) View of 3-D network arrangements along the *c* axis and along the *b* axis; (e-g) Simplified 3-D network of **Sm-MOF** based on the bridging Sm_2O_{18} nodes and BTB ligand.

3.2 Characterization of the Ln-MOFs and $CH_3NH_3PbBr_3$@Ln-MOFs composites

The peaks observed in the PXRD for the as-synthesized Ln-MOFs match well with the simulated patterns (**Figure S3a**), which indicated that the crystalline frameworks of the Ln-MOFs were maintained. On this basis, the PXRD of $CH_3NH_3PbBr_3$ and $CH_3NH_3PbBr_3$@Ln-MOFs composites were also tested. **Figure S3b** shows a comparison of the diffraction patterns of $CH_3NH_3PbBr_3$, **Ln-MOF**, $CH_3NH_3PbBr_3$@**Ln-MOF**, and $CH_3NH_3PbBr_3$@**Sm-MOF** at different concentrations. The extra diffraction peak (circled by the dotted green line) for the

$CH_3NH_3PbBr_3$@**Sm-MOF** agrees well with the main peak of $CH_3NH_3PbBr_3$, which is consistent with successful encapsulation. Moreover, the PXRD of **Sm-MOF** and $CH_3NH_3PbBr_3$@**Sm-MOF** were also tested at different temperatures in order to explore the thermal stability. **Sm-MOF** is stable to about 200 ℃ (**Figure 3a**), which is consistent with the TG curves (**Figure 3b**). Notably, $CH_3NH_3PbBr_3$@**Sm-MOF** can also be stabilized to 200 ℃ and a peak shift (circled by the dotted yellow line) was observed due to the breathing effect of the Sm-MOF after encapsulation of $CH_3NH_3PbBr_3$ on increasing the temperature[20] (**Figure 3c**).

The UV-Vis diffuse reflection spectra of H_3BTB, $CH_3NH_3PbBr_3$, Ln-MOFs, and $CH_3NH_3PbBr_3$@Ln-MOFs tested in the solid state at room temperature are shown in **Figure S4**. For all except $CH_3NH_3PbBr_3$, the peaks at 340 nm are attributed to the π-π* transitions of the triphenylbenzene of the BTB^{3-} ligand. Interestingly, the band edge at about 500 nm of $CH_3NH_3PbBr_3$@Ln-MOFs are blue shifted compared with the 520 nm of $CH_3NH_3PbBr_3$, which is thought to be due to the aggregation of $CH_3NH_3PbBr_3$ NPs in the solid state [21]. This provided further evidence for the successful encapsulation. Finally, the TEM images and the elemental mapping diagrams of $CH_3NH_3PbBr_3$@**Sm-MOF** at different concentrations of $PbBr_2$ (0.1mmol, 0.5mmol, 1mmol) confirmed the core-shell structures and good dispersity of $CH_3NH_3PbBr_3$ (**Figure 3d-f**). The size distributions illustrate that the size of $CH_3NH_3PbBr_3$ in $CH_3NH_3PbBr_3$@**Sm-MOF** at concentrations of $PbBr_2$ for 0.1, 0.5, and 1 mmol are in the ranges 0.2-1.0 nm, 0.3-1.2 nm and 0.2-1.3 nm, respectively (Figures S3c-e).

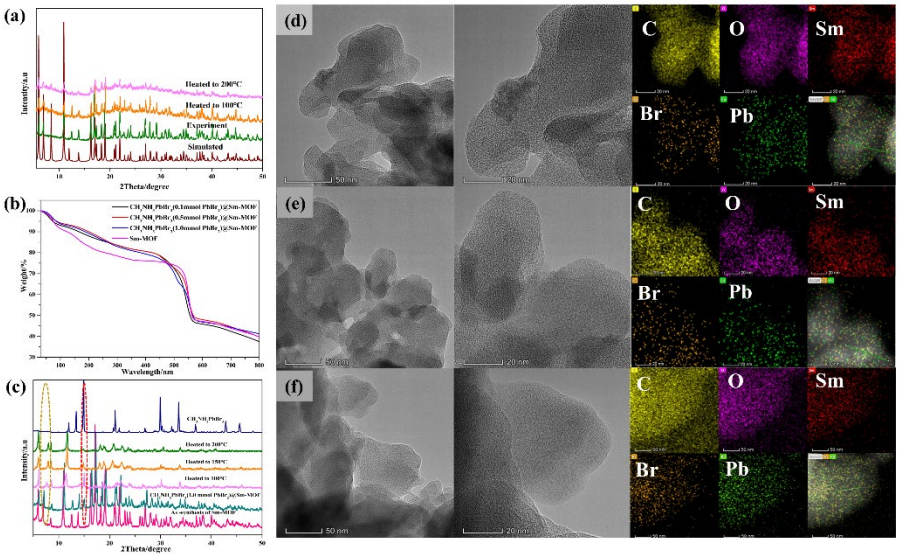

231

232 **Figure 3.** (a) PXRD patterns of Sm-MOF at variable temperature; (b)TG curves of Sm-
233 MOF and after encapsulated $CH_3NH_3PbBr_3$; (c) PXRD patterns of
234 $CH_3NH_3PbBr_3$@Sm-MOF at variable temperature; TEM image, elemental mapping
235 diagrams of (d) $CH_3NH_3PbBr_3$ (0.1 mmol $PbBr_2$)@**Sm-MOF**; (e) $CH_3NH_3PbBr_3$ (0.5
236 mmol $PbBr_2$)@**Sm-MOF**; (f) $CH_3NH_3PbBr_3$ (1.0 mmol $PbBr_2$)@**Sm-MOF**.

237

238 **3.3 Theoretical simulations**

239 The stability and electron transfer of this host-guest composite can be verified by
240 theoretical simulations based on density functional theory (DFT). The optimal
241 configuration of $CH_3NH_3PbBr_3$@**Sm-MOF** was obtained (**Figure 4a**), and the
242 differential charge density, energy band, as well as density of states (DOS) were
243 calculated. It turns out that the band value of the composite coated with perovskite
244 decreases visibly from 2.280 to 1.523 eV (**Figure 4b, c**), which reveals the conductivity
245 of the complex material increases and the potential barrier of the MOF itself in
246 $CH_3NH_3PbBr_3$@**Sm-MOF** decreases. The Pb-6s, C-2p, Br-4p and Sm-4f orbitals near
247 the fermi level (0 eV) provide possibilities for electron storage and transition (**Figure**
248 **4d**).

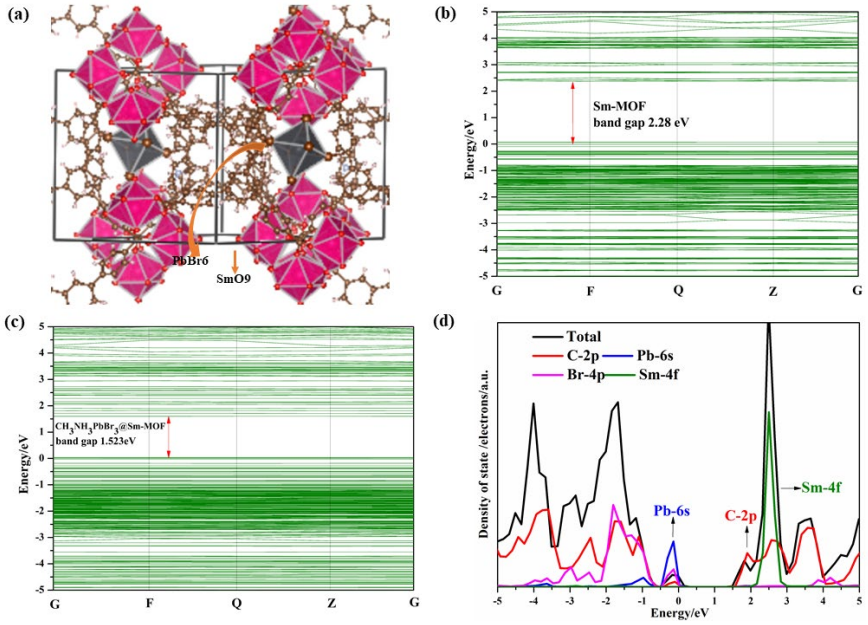

Figure 4. (a) Configuration optimization diagram of $CH_3NH_3PbBr_3$@**Sm-MOF**; (b) Band of Sm-MOF; (c) Band of $CH_3NH_3PbBr_3$@**Sm-MOF**; (d) DOS of $CH_3NH_3PbBr_3$@**Sm-MOF** and **Sm-MOF**.

Moreover, the charge transfer between $CH_3NH_3PbBr_3$ and **Sm-MOF** has been visualized by a differential charge density diagram (**Figure 5a**). Here, the blue areas of electron dissipation represent negative electrons, and the yellow areas represent positron aggregation. The N, Br in the $CH_3NH_3PbBr_3$ and the benzene ring in BTB form a p-π conjugate (**Figure 5b, 5c**), making the mutual repulsion between electrons decrease and the system energy reduces, and then the host-guest material becomes more stable. The conductivity of the conjugated organic molecule will improve after the HOMO or LUMO are partially filled [22]. Moreover, the electron rich behaviour of the Pb^{2+} ions can be seen in the enlarged differential charge density image at the reduced isosurface level (**Figure 5d**), which also proved the electron transfers from the ligand

in the host frame to the guest metal center.

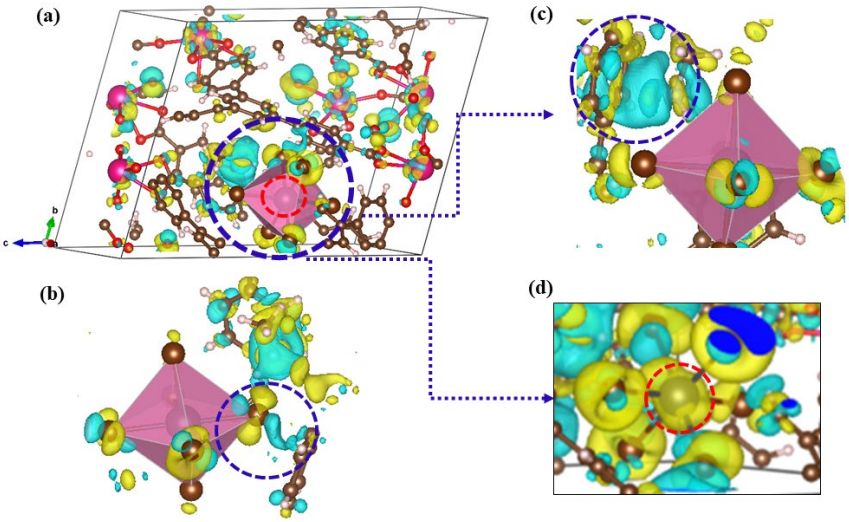

Figure 5. (a) The optimized geometry and differential charge density of $CH_3NH_3PbBr_3$@**Sm-MOF;** (b-d) Partially amplified charge density images.

3.4 Optical Properties and Tunable Luminescence

The room temperature luminescence of free $CH_3NH_3PbBr_3$, H_3BTB and Ln-MOFs were tested (**Figure S5**). For $CH_3NH_3PbBr_3$, there is a peak at 533 nm and green emission in solid state, which agrees with the reported observations [18a]. For the Ln-MOFs, the peaks at about 370 nm excited at 320 nm are the π–π* transitions of triphenylbenzene in the BTB ligands, and compare with free H_3BTB the shifts were dictated by their aggregated difference [23]; no characteristic peaks for La^{3+}, Pr^{3+} or Nd^{3+} ions were observed. In other words, no metal-centered emissions were detected. However, near IR adsorptions can be observed for **Sm-MOF** (**Figure 6a**), and these absorptions stem from excitation from ground states to the corresponding excited states of Sm^{3+} [24]. The characteristic peaks for Sm^{3+} at 561, 598, 643, and 703 nm correspond to $^4G_{5/2}\rightarrow{}^6H_{5/2}$, $^4G_{5/2}\rightarrow{}^6H_{7/2}$, $^4G_{5/2}\rightarrow{}^6H_{9/2}$, and $^4G_{5/2}\rightarrow{}^6H_{11/2}$, respectively [25]. The

maintenance of this characteristic fluorescence of Sm^{3+} in the Sm-MOF system was attributed to its excited state energy matching with the 3ππ* of the BTB^{3-} ligand [25-26]. The photographs showing the colour changes associated with the Ln-MOFs and solid $CH_3NH_3PbBr_3$ at room temperature illustrate the original luminous colour of the Ln-MOFs and luminescence quenching of $CH_3NH_3PbBr_3$ in the solid state (**Figure S6a**). It reveals that the temperature-dependent luminescence property of $CH_3NH_3PbBr_3$@Ln-MOFs. The peaks at about 370 nm were almost unaffected on reduction of the temperature. On the contrary, the characteristic emission peak of the perovskite clearly changes, which likely originates from the change of structural order and disorder phase transition at different temperature [27]. The $CH_3NH_3PbBr_3$@**La-MOF** generates green emission in the solid state at room temperature, exhibiting two peaks at 372 and 516 nm under excitation at 320 nm. On heating the temperature from 77 to 297 K, the intensity of the peak at 528 nm reduced gradually and blue shifted to 516 nm (**Figure S6b**). For $CH_3NH_3PbBr_3$@**Pr-MOF** at 77 K, green emission was observed with a maximum peak at about 545 nm under excitation at 320 nm. The intensity of this peak reduced gradually and blue shifted to 539 nm when the temperature increased to 177 K. On further heating to 297 K, the intensity of this peak gradually decreased and underwent a blue shift of 16 nm (**Figure S6c**). For $CH_3NH_3PbBr_3$@**Nd-MOF**, an additional new peak was observed at about 428 nm compared to the above two composites (**Figure S6d**). The intensity of this peak increases to the maximum with a slight blue shift on heating from 77 to 297 K. Furthermore, the intensity of the peak observed at ambient temperature at about 543

303 nm also decreases with a concomitant blue shift to 520 nm during the temperature
304 change to 297 K. The temperature-dependent luminescence of $CH_3NH_3PbBr_3$@**Sm-**
305 **MOF** reveals different luminescent behaviour (**Figure 6b, 6c**). In particular, a peak at
306 436 nm appears, whilst the peak at about 545 nm exhibits a slight blue shift as the
307 temperature rises to 297 K, attributed to the main emission peak of $CH_3NH_3PbBr_3$ been
308 more easily affected by temperature, and the characteristic emission peaks for Sm^{3+} at
309 598, 643 and 703 nm reveal slight intensity changes compared to the peaks of
310 $CH_3NH_3PbBr_3$. In general, electrons are concentrated at the bottom of the conduction
311 band, while holes are concentrated at the top of the valence band. The energy of emitting
312 electrons is basically equal to the width of the band gap, and the colour of the emission
313 depends on the width of the band gap [28]. This above blue shift of $CH_3NH_3PbBr_3$ in the
314 host-guest system is attributed to the widening of the band gap caused by the thermal
315 expansion of the $CH_3NH_3PbBr_3$ lattice, especially the lattice dilation term [29]. The
316 phase transition temperature (157 K) is similar to that reported in the literature (150 K)
317 [30]. Besides, the change of emission peak intensity of the same structure should be the
318 result of temperature dependent deformation of lattice [29b].

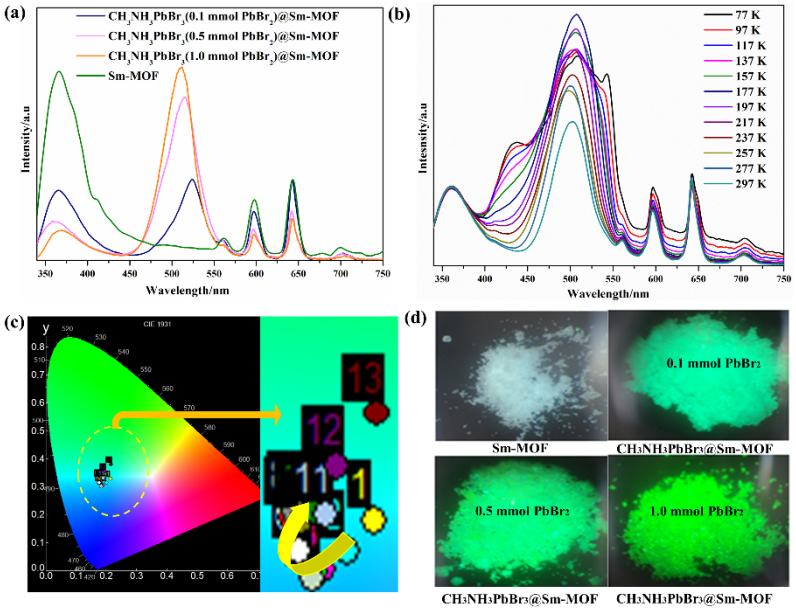

Figure 6. (a) Fluorescence spectra of $CH_3NH_3PbBr_3$@**Sm-MOF** with different concentration of $CH_3NH_3PbBr_3$ at room temperature; (b, c) Fluorescence emission spectra and CIE chromaticity coordinates (numbers 1 through 13 represent each temperature from 77 to 297 K) of $CH_3NH_3PbBr_3$@**Sm-MOF** over the temperature range 77 to 297 K; (d) Photographs of $CH_3NH_3PbBr_3$@**Sm-MOF** with different concentration of $CH_3NH_3PbBr_3$ under the UV light.

Meanwhile, following the encapsulation of $CH_3NH_3PbBr_3$, on addition of 1.0 mmol $PbBr_2$ as an example by the Ln-MOFs, there was a clear change in the luminescence. Here, **Sm-MOF** was selected as a platform for limiting perovskite with different concentrations because of its characteristic emission peaks. $CH_3NH_3PbBr_3$@**Sm-MOFs** with addition of 0.1, 0.5, and 1.0 mmol $PbBr_2$ were studied to explore the optical effects of concentrations of $CH_3NH_3PbBr_3$ encapsulation with **Sm-MOF**. Photographs of $CH_3NH_3PbBr_3$@**Sm-MOF** with different concentration of

$CH_3NH_3PbBr_3$ under the UV light show clear differences (**Figure 6d**). The result shows that the quantum yields (QY) improved upon increasing the concentration of $CH_3NH_3PbBr_3$ to 0.50, 0.62 and 0.98, respectively, which is higher than that of pure $CH_3NH_3PbBr_3$ (QY = 0.37) and **Sm-MOF** (QY = 0.42) in the solid state. The luminescence spectra of **Sm-MOF** and $CH_3NH_3PbBr_3$@**Sm-MOF** at different concentrations of $CH_3NH_3PbBr_3$ at room temperature show that the peak at 524 nm has blue shifted to 512 nm and increased, while the peaks at 370, 561, 598, 643 and 703 nm reduced slightly on increasing the concentration. In addition, to study the effect of higher temperatures on the luminescence, the $CH_3NH_3PbBr_3$@Ln-MOFs samples were heated from 307 to 457 K. From **Figure S7**, it was seen that both the peaks at about 370 and 520 nm gradually reduce, which suggests typical thermal quenching behaviour. However, the other characteristic emission peaks all relatively increase, due to the intensification of the energy transfer process consistent with the literature [31].

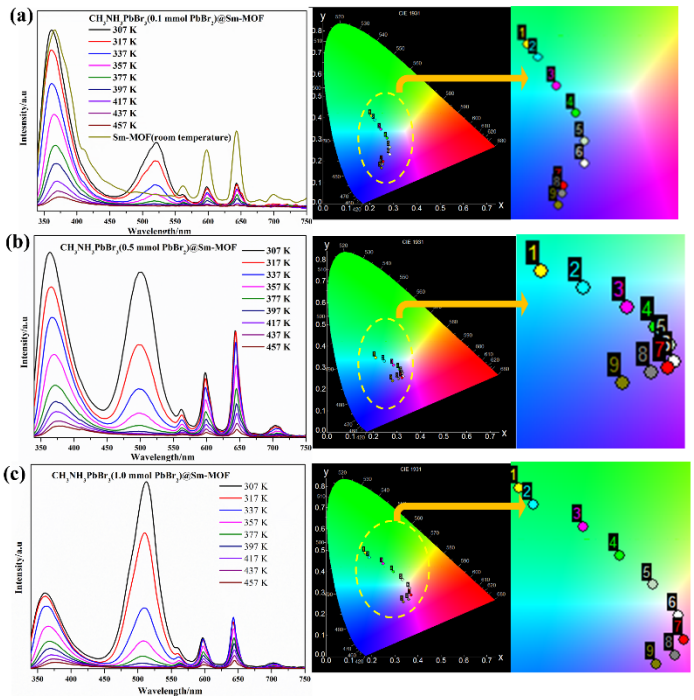

Figure 7. Fluorescence emission spectra of (a) $CH_3NH_3PbBr_3$@**Sm-MOF** (0.1 mmol

PbBr2); (b) $CH_3NH_3PbBr_3$@**Sm-MOF** (0.5 mmol PbBr2); (c) $CH_3NH_3PbBr_3$@**Sm-MOF** (1.0 mmol PbBr2) over the temperature range 307 to 457 K.

With the increase of temperature, the $CH_3NH_3PbBr_3$@**Sm-MOFs** with different concentrations of PbBr2 generate different emission spectra and different colours (**Figure 7**). The colour of the materials changes from green to blue-green and then to blue, green to purple and then to blue, green to yellow-green and then to purple for the addition of 0.1, 0.5 and 1.0 mmol PbBr2, respectively. Moreover, the decay times for $CH_3NH_3PbBr_3$@Ln-MOFs are all longer than those observed for the Ln-MOFs, H_3BTB as well as $CH_3NH_3PbBr_3$ (**Figure 8a**), caused by the non-radiative charge transfer between host and guest, which is a major problem in developing optoelectronic devices because of its central role in their performance [32]. As the content of $CH_3NH_3PbBr_3$ increases, the decay time extends (**Figure 8b**), which is attributed to the charge transfer and defect state reduction as increasing content of $CH_3NH_3PbBr_3$ [32b].

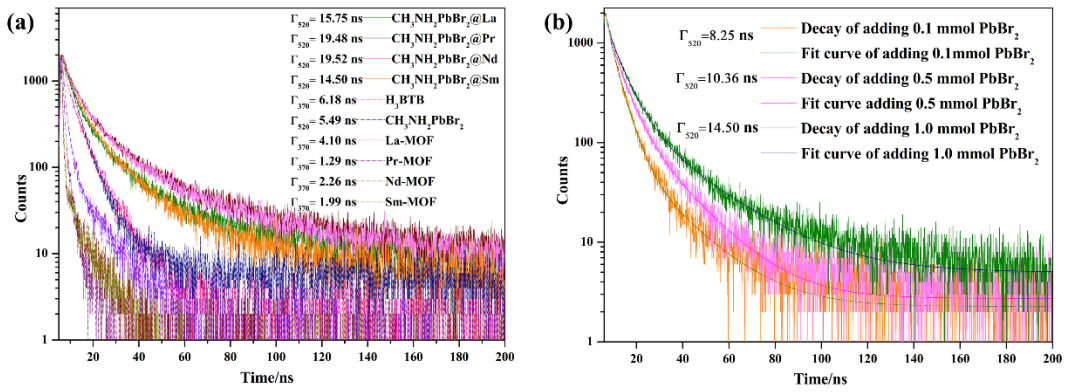

Figure 8. Time-resolved emission decay curves for (a) H3BTB, $CH_3NH_3PbBr_3$, Ln-MOF and $CH_3NH_3PbBr_3$@Ln-MOF; (b) at different concentrations.

3.5 Photocurrent Response Performances

Photocurrent response properties have rarely been detected in $CH_3NH_3PbBr_3$@Ln-MOFs composites, but have frequently been observed in composites such as Metal NPs@MOF [33], viologen-based metal halide hybrids [34] and in most other semiconductor p–n heterojunction devices [35]. Herein, the performance was recorded using a typical three-electrode system and the resulting photocurrent-time (I-T) curves with ON-OFF switch are presented in **Figure 9**. From **Figure 9a**, it is evident that the current intensity of Ln-MOFs is lower than that of corresponding $CH_3NH_3PbBr_3$@Ln-MOFs. The $CH_3NH_3PbBr_3$@**Sm-MOF** containing different amounts of $CH_3NH_3PbBr_3$ was also tested in order to explore the concentration dependence of the photocurrent intensity. It reveals that the intensity of the current increases as the concentration increases (**Figure 9b**). According to the recognized mechanism of photocurrent generation, irradiation can produce free radicals on organic groups including Ln-MOFs and $CH_3NH_3PbBr_3$, and then the electrons on the organic part move to the ITO substrate, generating a recyclable current. The increasing photocurrents after limiting $CH_3NH_3PbBr_3$ can be explained by their ability to act as efficient light absorbers and electron hole transport materials in photovoltaic devices [36]. The electrical bistability of the $CH_3NH_3PbBr_3$@**Sm-MOF** also implies the characteristics of charge hole separation.

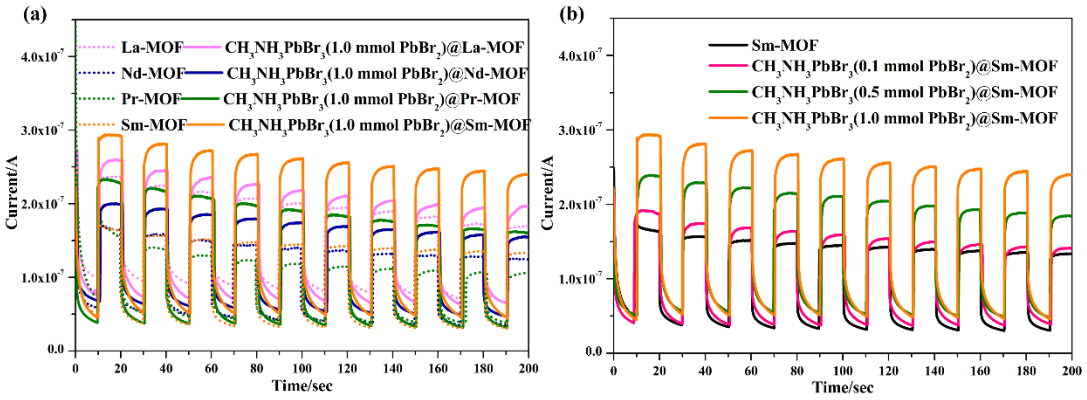

Figure 9. Photocurrent response performance of (a) $CH_3NH_3PbBr_3$@Ln-MOFs and (b) $CH_3NH_3PbBr_3$@**Sm-MOF** with different concentration of $PbBr_2$.

3.6 Electrical Bistability Behaviour

For the pure perovskite, it is found that the high resistance state of the device decreases with the increase of the number of cycles, and finally ends up close to the low resistance state, which leads to a small switch ratio. At the same time, the life cycle of the device depends on the erasing voltage. Moreover, the higher the voltage, the lower the life cycle (**Figure S8a**). This can be attributed to the continuous proliferation of halogen vacancies in the film during the cycle process. The activation energy of halogen vacancies will also decrease, inducing the abnormal reverse opening phenomenon of the device in the process of erasing. Finally, the overgrown halogen vacancy conductive channel cannot be effectively burned off by the erasable voltage, so that the device cannot return to the high resistance state and fail [19]. Similarly, electrical bistability is not found in pure **Sm-MOF** because of its higher barrier (**Figure S8b**). However, it is generally accepted that controlling the defect traps is an effective way to improve memory performance [37]. Owing to a certain potential barrier of the

main frame material, the charge transfer on the surface of the QDs is relatively stable, which avoids the defect of fast recombination of carriers when the applied electric field is removed, and shows the storage function. Therefore, when the perovskite is coated with the MOF, the formation of a halogen vacancy is prevented and the cyclic stability of the device is promoted. As **Figure 10a** shows, the ITO/$CH_3NH_3PbBr_3$@**Sm-MOF** (addition of 1.0 mmol $PbBr_2$) film displays the typical electrical hysteresis behaviour in a certain voltage sweep of 0V→-5V→0V→5V→0V, which is an essential feature for bistable memory devices. The cross-sectional images of this sandwich device were characterized by HR-SEM, and the thickness of the film was about 1.55 μm (**Figure 10b**). From the results (**Figure 10c**), it can be found that the film maintains high resistance state (HRS, OFF state) during the sweep from 0 to -5 V. Then the current suddenly converts to a low resistance state (LRS, ON state) at -5 V (ON: -5 V), which can be maintained with the voltage reversing from -5 to 5 V. The switches turn back to HRS when the voltage was reversed at 1.5 (OFF: 1.5 V), which can be maintained from 1.5→0 V. A similar I-V curve can be found in $CH_3NH_3PbBr_3$, the ON/OFF ratio is less than 1×10^2 and there is no electrical bistable signal for pure **Sm-MOF**. However, for the $CH_3NH_3PbBr_3$@**Sm-MOF**, the ON/OFF ratio of this device is 1×10^4, which presents a higher ON/OFF ratio. Moreover, the cycle stability was verified by 100 I-V cycle tests. It reveals that the ON/OFF ratio does not decrease significantly, confirming their cyclic stability (**Figure 10d**).

Generally speaking, the memristor mechanism of materials is usually attributed to the formation of a reversed space charge field within them [38]. Most of the previous

studies on the mechanism of electrical bistability were based on the resistance switching mechanism such as a conductive wire, a metal oxide interface, and space charge limited conduction (SCLC) [39]. Especially, the SCLC mechanism of capture control is closely related to the charge carrier trapping or detrapping in these host-guest composites. Based on our research perspective, SCLC is suitable to the I-V characteristics of these devices. The operating mechanism of these host-guest type electrical bistable storage materials can be summarized as follows. When a certain applied electric field is applied, the electric field shielding effect of the main frame is weakened, and the electrons transfer from the main frame to the guest molecule. In the absence of an applied electric field, because the ability of the guest molecule to release electrons changes, these electrons are stored in the guest molecule due to the enrichment of central Pb^{2+} ion and barrier in the host frame. However, when a reverse electric field is applied, the original equilibrium is broken and electrons tunnel from the guest molecule back to the host frame, thus realizing the conversion between the two steric hindrance states. The peaks of the Pb-6s and the C-2p orbital in the benzene ring proved the possibility of the electronic transition. Based on these results, the $CH_3NH_3PbBr_3$@Ln-MOF host-guest materials possesses stable memory storage capabilities.

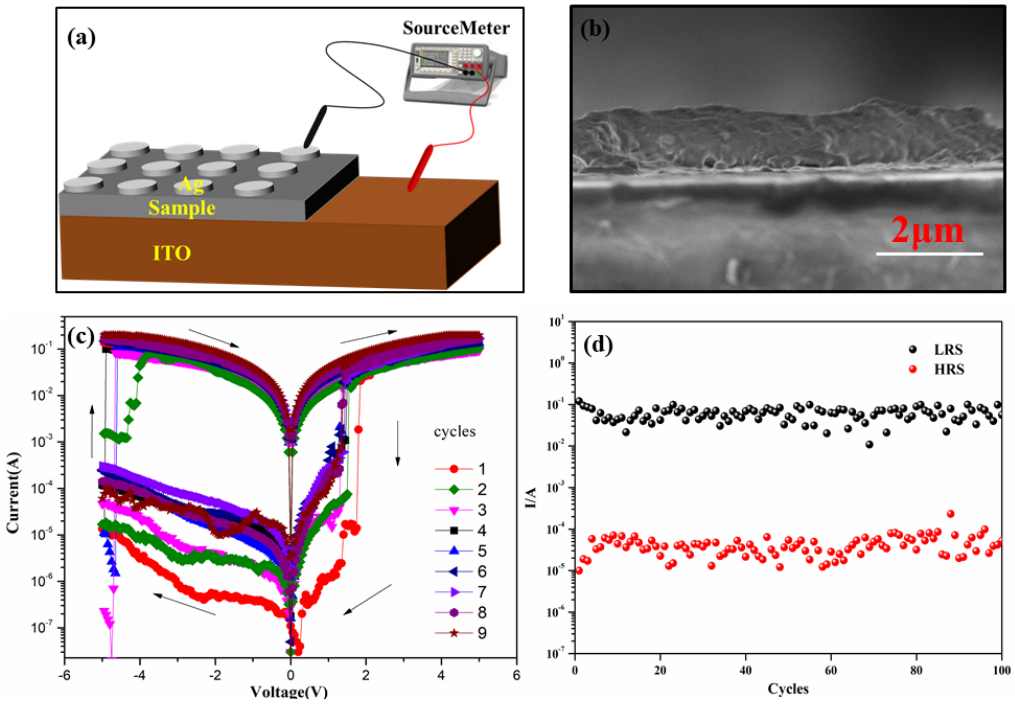

Figure 10 (a) Schematic illustration of the ITO/ Sample /Ag memory device; (b) Cross-sectional SEM images; (c) I-V characteristics of the ITO/$CH_3NH_3PbBr_3$@**Sm-MOF**; (d) Cycle endurance of the ITO/$CH_3NH_3PbBr_3$@**Sm-MOF**.

4. Conclusions

In summary, $CH_3NH_3PbBr_3$ NPs were encapsulated into a family of Ln-MOFs, serving as potential tuneable luminescent, photovoltaic, and memory storage devices. The results show that the luminescence behaviour was readily adjusted, the most obvious feature was the modulation from blue to green and the fluorescence life was longer than that of the precursor materials. In the case of $CH_3NH_3PbBr_3$@**Sm-MOF**, it has characteristics of variable lifetime and adjustable luminescence between green, blue and purple controlled by either the temperature or loading concentration. Moreover, the photocurrent test revealed the superiority of these host-guest materials by changing the

concentration of the encapsulated $CH_3NH_3PbBr_3$. Interestingly, the $CH_3NH_3PbBr_3$@**Sm-MOF** shows electrical bistable behaviour. The ON/OFF ratio of this device is up to 1×10^4, which is attributed to the better electrical conductivity of the perovskite and the structural characteristics of the outermost electrons of the lanthanide metals. The encapsulated $CH_3NH_3PbBr_3$ NPs improves the electron tunnelling efficiency, making it a potential memory storage device.

Declaration of Competing Interest

The authors declare that they have no known competing financial interests or personal relationships that could have appeared to influence the work reported in this paper.

Acknowledgements

This work was financially supported by National Natural Science Foundation of China (NOS: 21771038), National Natural Science Foundation of Fujian Province (2018J01684, 2017J01409) China scholarship council foundation. CR thanks the University of Hull for support.

Appendix A. Supplementary data

Supplementary data to this article can be found online at XXX.

References

[1] a) A. Vartanian, *Nature Reviews Materials* **2022**, 7, 257; b) M. Bonneau, C. Lavenn, J.-J. Zheng, A. Legrand, T. Ogawa, K. Sugimoto, F.-X. Coudert, R. Reau, S. Sakaki, K.-i. Otake, S. Kitagawa, *Nature Chemistry* **2022**, DOI: 10.1038/s41557-022-

00928-x; c) P. Peng, A. Anastasopoulou, K. Brooks, H. Furukawa, M. E. Bowden, J. R. Long, T. Autrey, H. Breunig, *Nature Energy* **2022**, DOI: 10.1038/s41560-022-01013-w; d) J. Fonseca, T. Gong, L. Jiao, H.-L. Jiang, *Journal of Materials Chemistry A* **2021**, 9, 10562; e) L. Yan, A. Gopal, S. Kashif, P. Hazelton, M. Lan, W. Zhang, X. Chen, *Chemical Engineering Journal* **2022**, 435, 134975.

[2] Y. Zheng, C.-S. Cao, W. Ma, T. Chen, B. Wu, C. Yu, Z. Huang, J. Yin, H.-S. Hu, J. Li, W.-X. Zhang, Z. Xi, *Journal of the American Chemical Society* **2020**, 142, 10705.

[3] a) W.-T. Koo, S.-J. Kim, J.-S. Jang, D.-H. Kim, I.-D. Kim, *Advanced Science* **2019**, 6, 1970126; b) B. Gole, U. Sanyal, R. Banerjee, P. S. Mukherjee, *Inorganic Chemistry* **2016**, 55, 2345; c) W.-T. Koo, S.-J. Kim, J.-S. Jang, D.-H. Kim, I.-D. Kim, *Advanced Science* **2019**, 6, 1900250; d) J. Li, Z. Xu, T. Wang, X. Xie, D. Li, J. Wang, H. Huang, Z. Ao, *Chemical Engineering Journal* **2022**, DOI: https://doi.org/10.1016/j.cej.2022.136900136900.

[4] a) M. Li, G. Ren, W. Yang, Y. Yang, W. Yang, Y. Gao, P. Qiu, Q. Pan, *Chemical Communications* **2021**, 57, 1340; b) Z. Wang, C.-Y. Zhu, J.-T. Mo, P.-Y. Fu, Y.-W. Zhao, S.-Y. Yin, J.-J. Jiang, M. Pan, C.-Y. Su, *Angewandte Chemie International Edition* **2019**, 58, 9752.

[5] a) M. Duguet, A. Lemarchand, Y. Benseghir, P. Mialane, M. Gomez-Mingot, C. Roch-Marchal, M. Haouas, M. Fontecave, C. Mellot-Draznieks, C. Sassoye, A. Dolbecq, *Chemical Communications* **2020**, 56, 10143; b) C. T. Buru, O. K. Farha, *ACS Applied Materials & Interfaces* **2020**, 12, 5345; c) C. T. Buru, P. Li, B. L.

503 Mehdi, A. Dohnalkova, A. E. Platero-Prats, N. D. Browning, K. W. Chapman, J. T.
504 Hupp, O. K. Farha, *Chemistry of Materials* **2017**, 29, 5174; d) D. Cao, Q. Sha, J.
505 Wang, J. Li, J. Ren, T. Shen, S. Bai, L. He, Y.-F. Song, *ACS Applied Materials &*
506 *Interfaces* **2022**, DOI: 10.1021/acsami.2c04077; e) P. Mialane, C. Mellot-
507 Draznieks, P. Gairola, M. Duguet, Y. Benseghir, O. Oms, A. Dolbecq, *Chemical*
508 *Society Reviews* **2021**, 50, 6152; f) G. Ye, L. Hu, Y. Gu, C. Lancelot, A. Rives, C.
509 Lamonier, N. Nuns, M. Marinova, W. Xu, Y. Sun, *Journal of Materials Chemistry*
510 *A* **2020**, 8, 19396.
511 [6] a) J. Yan, Y. Cui, M. Xie, G.-Z. Yang, D.-S. Bin, D. Li, *Angewandte Chemie*
512 *International Edition* **2021**, 60, 24467; b) S. Subudhi, S. P. Tripathy, K. Parida,
513 *Inorganic Chemistry Frontiers* **2021**, 8, 1619.
514 [7] a) D. Rambabu, S. Bhattacharyya, T. Singh, C. M. L, T. K. Maji, *Inorganic*
515 *Chemistry* **2020**, 59, 1436; b) L.-Y. Wu, Y.-F. Mu, X.-X. Guo, W. Zhang, Z.-M.
516 Zhang, M. Zhang, T.-B. Lu, *Angewandte Chemie International Edition* **2019**, 58,
517 9491; c) S. Liu, J. Zhou, Z. Cai, G. Fang, Y. Cai, A. Pan, S. Liang, *Journal of*
518 *Materials Chemistry A* **2016**, 4, 17838; d) C. Ren, Z. Li, L. Huang, X. Xiong, Z.
519 Nie, Y. Yang, W. Zhu, W. Yang, L. Wang, *Nanoscale* **2022**, 14, 4216; e) A. E. B. S.
520 Stone, S. Irgen-Gioro, R. López-Arteaga, J. T. Hupp, E. A. Weiss, *Chemistry of*
521 *Materials* **2022**, 34, 1921.
522 [8] T. Xia, Z. Shao, X. Yan, M. Liu, L. Yu, Y. Wan, D. Chang, J. Zhang, D. Zhao,
523 *Chemical Communications* **2021**, 57, 3143.
524 [9] Y. Zhang, M. Gutiérrez, A. K. Chaudhari, J.-C. Tan, *ACS Applied Materials &*

525 *Interfaces* **2020**, 12, 37477.

526 [10] J. Yu, Y. Cui, C.-D. Wu, Y. Yang, B. Chen, G. Qian, *Journal of the American*
527 *Chemical Society* **2015**, 137, 4026.

528 [11] T. Wu, X. Liu, Y. Liu, M. Cheng, Z. Liu, G. Zeng, B. Shao, Q. Liang, W. Zhang,
529 Q. He, W. Zhang, *Coordination Chemistry Reviews* **2020**, 403, 213097.

530 [12] K. Kumagai, T. Uematsu, T. Torimoto, S. Kuwabata, *Chemistry of Materials* **2021**,
531 33, 1607.

532 [13] J. Cuan, D. Zhang, W. Xing, J. Han, H. Zhou, Y. Zhou, *Chemical Engineering*
533 *Journal* **2021**, 425, 131556.

534 [14] Q. Yang, Q. Wang, Y. Long, F. Wang, L. Wu, J. Pan, J. Han, Y. Lei, W. Shi, S.
535 Song, *Advanced Energy Materials* **2020**, 10, 1903193.

536 [15] T. Xuan, X. Yang, S. Lou, J. Huang, Y. Liu, J. Yu, H. Li, K.-L. Wong, C. Wang, J.
537 Wang, *Nanoscale* **2017**, 9, 15286.

538 [16] L. Liu, A. Najar, K. Wang, M. Du, S. Liu, *Advanced Science* **2022**, 9, 2104577.

539 [17] R. A. John, N. Yantara, S. E. Ng, M. I. B. Patdillah, M. R. Kulkarni, N. F.
540 Jamaludin, J. Basu, Ankit, S. G. Mhaisalkar, A. Basu, N. Mathews, *Advanced*
541 *Materials* **2021**, 33, 2007851.

542 [18] a) D. Zhang, W. Zhou, Q. Liu, Z. Xia, *ACS Applied Materials & Interfaces* **2018**,
543 10, 27875; b) D. Zhang, Y. Xu, Q. Liu, Z. Xia, *Inorganic Chemistry* **2018**, 57,
544 4613; c) J. Ren, T. Li, X. Zhou, X. Dong, A. V. Shorokhov, M. B. Semenov, V. D.
545 Krevchik, Y. Wang, *Chemical Engineering Journal* **2019**, 358, 30.

546 [19] Y. Ren, H. Ma, W. Wang, Z. Wang, H. Xu, X. Zhao, W. Liu, J. Ma, Y. Liu,

Advanced Materials Technologies **2019**, 4, 1800238.

[20] C. Volkringer, T. Loiseau, N. Guillou, G. Férey, E. Elkaïm, A. Vimont, *Dalton Transactions* **2009**, DOI: 10.1039/B817563B2241.

[21] P. Bansal, P. Kar, *Journal of Luminescence* **2019**, 215, 116609.

[22] a) T. Oyamada, H. Tanaka, K. Matsushige, H. Sasabe, C. Adachi, *Applied Physics Letters* **2003**, 83, 1252; b) X. L. Mo, G. R. Chen, Q. J. Cai, Z. Y. Fan, H. H. Xu, Y. Yan, J. Yang, H. H. Gu, Z. Y. Hua, *Thin Solid Films* **2003**, 436, 259.

[23] Y. He, Z. Bian, C. Kang, Y. Cheng, L. Gao, *Tetrahedron* **2010**, 66, 3553.

[24] L.-M. Zhao, X.-Q. Shen, Q. Liu, W. Wu, H.-H. Li, Z.-R. Chen, Y. Li, *Chemistry – An Asian Journal* **2020**, 15, 136.

[25] R. Deng, J. Yu, H. Zhang, L. Zhou, Z. Peng, Z. Li, Z. Guo, *Chemical Physics Letters* **2007**, 443, 258.

[26] Q. Wang, L. Tao, X. Jiang, M. Wang, Y. Shen, *Applied Surface Science* **2019**, 465, 607.

[27] H. Yu, W. Wu, Q. Wang, J. Liu, D. Kong, Y. Gao, *Materials Today Physics* **2022**, 22, 100621.

[28] M. Humayun, A. Zada, Z. Li, M. Xie, X. Zhang, Y. Qu, F. Raziq, L. Jing, *Applied Catalysis B: Environmental* **2016**, 180, 219.

[29] a) R. Saxena, J. Kangsabanik, A. Kumar, A. Shahee, S. Singh, N. Jain, S. Ghorui, V. Kumar, A. V. Mahajan, A. Alam, D. Kabra, *Physical Review B* **2020**, 102, 081201; b) M. I. Dar, G. Jacopin, S. Meloni, A. Mattoni, N. Arora, A. Boziki, S. M. Zakeeruddin, U. Rothlisberger, M. Grätzel, *Science Advances* **2016**, 2,

569 e1601156.
570 [30] Y. Liu, H. Lu, J. Niu, H. Zhang, S. Lou, C. Gao, Y. Zhan, X. Zhang, Q. Jin, L.
571 Zheng, *AIP Advances* **2018**, 8, 095108.
572 [31] J. Liu, Y. Zhuang, L. Wang, T. Zhou, N. Hirosaki, R. J. Xie, *Acs Appl Mater*
573 *Interfaces* **2018**, acsami.7b13486.
574 [32] a) X. Zhang, Z. Shao, X. Zhang, Y. He, J. Jie, *Advanced Materials* **2016**, 28, 10409;
575 b) I.-W. Cho, M.-Y. Ryu, *APL Materials* **2019**, 7, 051112.
576 [33] L. Zhao, W. Wu, X. Shen, Q. Liu, Y. He, K. Song, H. Li, Z. Chen, *ACS Applied*
577 *Materials & Interfaces* **2019**, 11, 47073.
578 [34] a) X. Yang, M. Giorgi, H. Karoui, D. Gigmes, V. Hornebecq, O. Ouari, A.
579 Kermagoret, D. Bardelang, *Chemical Communications* **2019**, 55, 13824; b) S.
580 Chen, L. Zhao, J. Ma, Y. Wang, L. Dai, J. Zhang, *Nano Energy* **2019**, 60, 536.
581 [35] a) M. Berdakin, E. A. Rodríguez-Mena, L. E. F. Foa Torres, *Nano Letters* **2021**,
582 21, 3177; b) Y. Yang, *Nature Electronics* **2021**, 4, 631; c) D. Wang, X. Liu, Y.
583 Kang, X. Wang, Y. Wu, S. Fang, H. Yu, M. H. Memon, H. Zhang, W. Hu, Z. Mi,
584 L. Fu, H. Sun, S. Long, *Nature Electronics* **2021**, 4, 645.
585 [36] a) P. Cottingham, D. C. Wallace, K. Hu, G. Meyer, T. M. McQueen, *Chemical*
586 *Communications* **2015**, 51, 7309; b) T. Zhu, Y. Yang, K. Gu, C. Liu, J. Zheng, X.
587 Gong, *ACS Applied Materials & Interfaces* **2020**, 12, 51744.
588 [37] a) J.-S. Lee, Y.-M. Kim, J.-H. Kwon, H. Shin, B.-H. Sohn, J. Lee, *Advanced*
589 *Materials* **2009**, 21, 178; b) D. Lee, B. Hwang, J.-S. Lee, *ACS Applied Materials*
590 *& Interfaces* **2019**, 11, 20225.

[38] Y.-R. Huang, X.-L. Lin, B. Chen, H.-D. Zheng, Z.-R. Chen, H.-H. Li, S.-T. Zheng, *Angewandte Chemie International Edition* **2021**, 60, 16911.

[39] a) *Nature Communications*; b) F. Paul, S. Paul, *Small* n/a, 2106442.